

Dissecting the Mid-Infrared Heart of M83 with JWST

SVEA HERNANDEZ ¹, LOGAN JONES,² LINDA J. SMITH ², ADITYA TOGI ³, ALESSANDRA ALOISI ²,
WILLIAM P. BLAIR ⁴, ALEC S. HIRSCHAUER ², LESLIE K. HUNT,⁵ BETHAN L. JAMES ¹, NIMISHA KUMARI,¹
VIANNEY LEBOUTELLER ⁶, MATILDE MINGOZZI ² AND LISE RAMAMBASON ⁷

¹*AURA for ESA, Space Telescope Science Institute, 3700 San Martin Drive, Baltimore, MD 21218, USA*

²*Space Telescope Science Institute, 3700 San Martin Drive, Baltimore, MD 21218, USA*

³*Texas State University, Department of Physics, 601 University Dr, San Marcos, TX 78666, USA*

⁴*The William H. Miller III Department of Physics and Astronomy, Johns Hopkins University, 3400 N. Charles Street, Baltimore, MD, 21218; wblair@jhu.edu*

⁵*INAF - Osservatorio Astrofisico di Arcetri, Largo E. Fermi 5, 50125 Firenze, Italy*

⁶*AIM, CEA, CNRS, Université Paris-Saclay, Université Paris Diderot, Sorbonne Paris Cité, F-91191 Gif-sur-Yvette, France*

⁷*Institut für Theoretische Astrophysik, Zentrum für Astronomie, Universität Heidelberg, Albert-Ueberle-Str. 2, D-69120 Heidelberg, Germany*

ABSTRACT

We present a first look at the MRS observations of the nucleus of the nearby galaxy M83, taken with MIRI onboard JWST. The observations show a rich set of emission features from the ionized gas, warm molecular gas, and dust. To begin dissecting the complex processes in this part of the galaxy, we divide the observations into four different regions. We find that the strength of the emission features varies strongly from region to region, with the south-east region displaying the weakest features tracing the dust continuum and ISM properties. Comparison between the cold molecular gas traced by the ¹²CO (1-0) transition with ALMA and the H₂ S(1) transition shows a similar spatial distribution. This is in contrast to the distribution of the much warmer H₂ emission from the S(7) transition found to be concentrated around the optical nucleus. We use the rotational emission lines and model the H₂ excitation to estimate a total molecular gas mass accounting for the warm H₂ component of $M(>50 \text{ K})_{\text{H}_2} = 67.90 (\pm 5.43) \times 10^6 M_{\odot}$. We compare this value to the total gas mass inferred by probing the cold H₂ gas through the ¹²CO (1-0) emission, $M(\text{CO})_{\text{H}_2} = 17.15 \times 10^6 M_{\odot}$. We estimate that $\sim 75\%$ of the total molecular gas mass is contained in the warm H₂ component. We also identify [O IV] 25.89 μm and [Fe II] 25.99 μm emission. We propose that the diffuse [Fe II] 25.99 μm emission might be tracing shocks created during the interactions between the hot wind produced by the starburst and the much cooler ISM above the galactic plane. More detailed studies are needed to confirm such a scenario.

1. INTRODUCTION

Starburst galaxies are ideal laboratories for studying the physics of star formation (SF) and overall galaxy evolution. These galaxies are commonly forming stars at a much higher rate than typical star-forming systems (e.g., SF rate per unit area $I_{\text{SF}} = 1\text{-}100 M_{\odot} \text{ yr}^{-1} \text{ kpc}^{-2}$; Heckman 1994; Meurer et al. 1997). Overall, starburst galaxies cover a broad range in morphology from blue compact dwarfs (BCDs, which share common properties with the high- z environments; e.g., Izotov et al. 2021) to spiral galaxies and merging systems (Leitherer & Heckman 1995; Leitherer et al. 1995; Annibali & Tosi 2022). Starbursts are believed to be a critical component in the evolution of galaxies as these are connected to processes such as the fueling of active galactic nuclei

(AGN; Knapen 2004), production of large populations of massive stars and massive star clusters (Meurer et al. 1995; Ho & Filippenko 1996; Adamo et al. 2010; Zhang et al. 2018), and powerful stellar/AGN outflows (Heckman et al. 1990; Rupke 2018; Cairós et al. 2022; Yuan et al. 2022). Due to the nature of starburst galaxies, several studies have suggested (Robertson et al. 2013, 2015; Finkelstein et al. 2019), and confirmed, that these compact systems could have been dominant contributors in the reionization of the Universe (Madau 1991; Heckman et al. 2011; Izotov et al. 2018a,b; Flury et al. 2022a,b; Marques-Chaves et al. 2022). Furthermore, these systems are believed to be responsible for $\sim 25\%$ of the star-formation rate on the high-mass end in the local universe, and dominate the star-forming activity at high redshift ($z > 0.7$; Heckman 1998; Le Floch et al. 2005).

Starbursts in these star-forming systems are generally located in smaller regions of a galaxy; in the case of large spirals these are located in the very central regions and are known as starburst nuclei (e.g., Balzano 1983).

Previous generations of infrared (IR) telescopes such as the Infrared Space Observatory (ISO) and the more recent Spitzer Space Telescope (Werner et al. 2004) have highlighted the complexity and richness of the mid-IR (MIR) observations of starburst nuclei (Genzel & Cesarsky 2000; Armus et al. 2004, 2006; Lahuis et al. 2007; Armus et al. 2020). Studies analyzing spectroscopic observations taken with the Infrared Spectrograph (IRS; Houck et al. 2004) on Spitzer uncovered strong atomic emission lines, many arising from highly-ionized gas (e.g., [Ne V]; Armus et al. 2007), polycyclic aromatic hydrocarbons (PAH) emission from dust grains (Brandl et al. 2006; Smith et al. 2007), strong emission from the warm molecular gas (H_2 ; Armus et al. 2006; Appleton et al. 2006; Stierwalt et al. 2014), and intense [Fe II] emission indicating the presence of shocks (Inami et al. 2013). The MIR understanding of starburst nuclei, and starbursting galaxies in general, will be revolutionized with the recent arrival of the James Webb Space Telescope (JWST). The medium resolution spectrometer (MRS) on the JWST Mid-Infrared Instrument (MIRI) is already allowing for studies of the detailed properties of these objects at spatial scales seven times smaller, fifty times more sensitive, and with spectral resolutions five times higher than those provided by the IRS on Spitzer (Rieke et al. 2015; Labiano et al. 2021; Sandstrom et al. 2022; Leroy et al. 2022; Thilker et al. 2023).

At a distance of 4.6 Mpc (Saha et al. 2006), M83 is the nearest face-on spiral galaxy. The confirmed central starburst (Díaz et al. 2006; Dopita et al. 2010), its orientation, and its metallicity ($\sim 1 - 3 Z_{\odot}$, with a high level of chemical enrichment e.g., Bresolin & Kennicutt 2002; Bresolin et al. 2016; Hernandez et al. 2021), make this galaxy an ideal environment to study in detail the MIR emission properties of starburst nuclei. The interest in the nucleus of M83 has increased as past studies have suggested that the ongoing starburst was most likely triggered by a recent minor merger (Knapen et al. 2010). This spiral galaxy has been studied extensively at a broad range of wavelengths: ultraviolet (UV; James et al. 2014; Hernandez et al. 2019, 2021; Bruzzone et al. 2020), optical (Mast et al. 2006; Kim et al. 2012; Blair et al. 2014), IR (Thatte et al. 2000; Knapen et al. 2010; Williams et al. 2015; Wu et al. 2015), radio (Maddox et al. 2006; Russell et al. 2020), and X-ray (Ducci et al. 2013; Long et al. 2014; Hunt et al. 2021; Wang et al. 2021). The starburst nucleus has shown to be a com-

plex system with a reported double ring structure (e.g., Elmegreen et al. 1998). Additionally, through analysis of three-dimensional spectroscopy data in the R band, studies have found that the nucleus of the galaxy is offset from its photometric and kinematic center by $4''$, which has been interpreted as evidence for a second nucleus (Thatte et al. 2000; Sakamoto et al. 2004; Mast et al. 2006; Díaz et al. 2006; Rodrigues et al. 2009) or as the result of a perturbation in the gravitational potential from a possible past interaction (Houghton & Thatte 2008).

Being a site of vigorous star formation, the nucleus of M83 is an excellent object to be studied in the MIR to uncover the processes fueling star formation and the complex interplay between star formation, ionized gas, and dust (both in emission and absorption). Here we report on new MIR integral field spectroscopy of the core of M83 taken with the MRS mode of MIRI onboard JWST and focus on two specific components: (1) the molecular gas component, and (2) possible evidence and origin of shocks. We highlight that future studies will further explore the MIRI/MRS observations expanding on the physical and chemical properties of the multiphase ISM and dust components in the nuclear regions of M83 (Jones et al. in prep.). This paper is structured as follows: In Section 2 we present a description of the new MIRI/MRS observations and data reduction, in Section 3 we describe the mid-infrared properties of the core of M83, and in Sections 4 and 5 we present a discussion of the observed properties and a brief summary, respectively. As an initial note, we highlight that all of the molecular gas masses discussed in this work refer to the H_2 masses, with no heavy element correction.

2. OBSERVATIONS AND DATA REDUCTION

The JWST observations presented in this paper were collected as part of Cycle 1 under PID 02219 (PI: Hernandez) between July 5 and 9, 2022. Given the expected pointing accuracy of JWST ($\sim 0.10''$), the program did not require a target acquisition. The M83 observations were taken with the MIRI/MRS instrument to create a 2×2 mosaic which fully sampled the entire nucleus of this nearby galaxy primarily with the largest MRS channel 4 (with a field of view, FOV, of $6.9'' \times 7.9''$ per pointing, see Figure 1). A 4-point dither pattern optimized for extended sources was also applied to achieve optimal sampling throughout the MRS FOV and to identify and remove detector artifacts. The individual pointings were strategically positioned to fully sample the massive stellar clusters with all four MIRI/MRS channels. To avoid data excess problems the observations were divided into three separate visits, each observing with a

different grating, SHORT (A), MEDIUM (B), LONG (C), to obtain contiguous wavelength coverage from ~ 5 to $28 \mu\text{m}$. Each pointing was observed with 40 groups per integration for a total of five integrations and a total exposure time of 2264 sec. Additionally, to accurately measure and correct for the thermal background, the program collected companion background MRS cubes avoiding contamination from the disk of the galaxy with identical integrations as those of the individual pointings.

The MIRI/MRS raw products were retrieved from the Mikulski Archive for Space Telescopes (MAST). The observations were reduced with the JWST calibration software version (CAL_VER) 1.6.2. We also applied residual fringe corrections available in the JWST pipeline to both the three-dimensional and one-dimensional observations, in the latter taking care of the low-level dichroic fringing pattern. All the *JWST* data used in this paper can be found in MAST: [10.17909/a61h-f081](https://mast.stsci.org/portal/#/data/10.17909/a61h-f081).

3. RESULTS

Our MIRI/MRS observations roughly cover the core of M83 in a region of approximately $200 \text{ pc} \times 200 \text{ pc}$. To begin dissecting the complex processes taking place in this part of the galaxy, we divided the nucleus of M83 into four different regions primarily following the individual MIRI/MRS pointings (see Figure 1). We extracted a single spectrum per region (per channel) and correct for foreground extinction adopting the latest MIR extinction curve by [Gordon et al. \(2021\)](#). Given that the different channels have slightly different FOVs, we scaled the extracted spectra for channels 2, 3 and 4 to the continuum of those from channel 1 between 5.57 and $5.59 \mu\text{m}$, a particularly featureless wavelength range. The corrected spectra analyzed in this work are shown in Figure 2.

All four regions in the nucleus of M83 exhibit both strong and weak PAH emission features (6.2 , 7.7 , 8.6 , 11.3 , 12.0 , 12.7 , 13.5 , 14.2 , 16.4 , 17.4 , $17.8 \mu\text{m}$, highlighted by the bottom grey arrows in Figure 2). We list in Table 1 the inferred fluxes for some of the strongest PAH features in the different regions. These initial measurements were done with the PAHFIT software ([Smith et al. 2007](#)). The spectra are also rich in emission from fine-structure lines such as [Fe II] $5.34 \mu\text{m}$, [Fe III] $22.93 \mu\text{m}$, [Fe II] $25.99 \mu\text{m}$, [Ar II] $6.99 \mu\text{m}$, [Ar III] $8.99 \mu\text{m}$, [S III] $18.71 \mu\text{m}$, [S IV] $10.51 \mu\text{m}$, [Ne II] $12.81 \mu\text{m}$, [Ne III] $15.56 \mu\text{m}$, [Cl II] $14.37 \mu\text{m}$, and [O IV] $25.89 \mu\text{m}$, as well as hydrogen recombination lines (P α $7.46 \mu\text{m}$, H α $7.50 \mu\text{m}$, H α $12.37 \mu\text{m}$) with strengths varying from region to region. In Table 2 we list the foreground extinction-corrected fluxes for a broad range

of emission lines, along with their corresponding full width at half maximum (FWHM). Finally, we also detect emission from seven H₂ 0-0 rotational lines, S(1) through S(7), and similar to the fine-structure lines, the emission from the warm molecular gas appears to vary strongly from region to region (see Table 3 for a list of foreground extinction-corrected H₂ flux measurements). Specifically for these H₂ lines we observe velocity shifts of the order of $\sim 100 \text{ km s}^{-1}$ from Region 1 to region 4, comparable to values in the the velocity maps by [Callanan et al. \(2021\)](#). Many of these lines have been previously detected in Spitzer/IRS spectra (e.g., PI: Rieke, PID: 59); however, the higher spectral resolution of the MIRI/MRS observations allow us to analyze the distribution and dynamics of the molecular and atomic gas, as well as dust, in a spatially-resolved manner at spatial scales of $\sim 100 \text{ pc}$ in the present study, and we plan to explore the physical properties of these regions at the spatial scales of a few tens of pc in future studies.

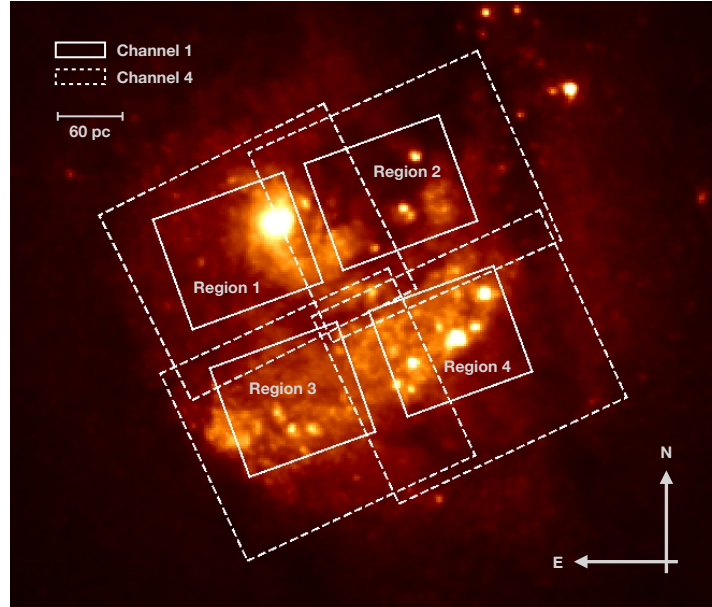


Figure 1. HST/WFC3 (F110W, resolution $\sim 0.11''$, PID: 11360) image of the core of M83. We show with white boxes the location of the JWST MIRI/MRS Channel 1 (solid) with coverage at short wavelengths ($5\text{--}8\ \mu\text{m}$) and Channel 4 (dashed), with full coverage at longer wavelengths ($17\text{--}28\ \mu\text{m}$). The labels in each quadrant are the adopted regions throughout our analysis.

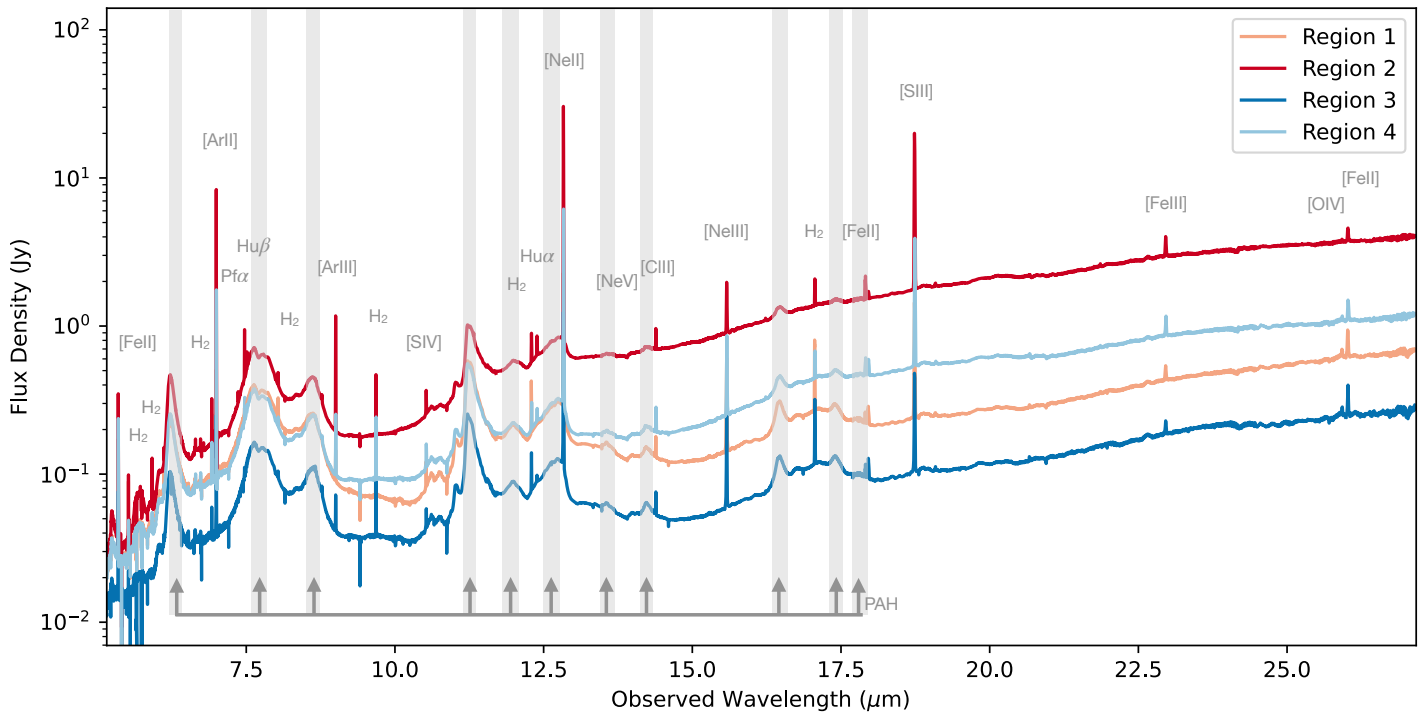


Figure 2. Mid-infrared spectra of four different regions in the nucleus of M83 as observed by JWST/MIRI. Note that the spectra from the MIRI/MRS Channels 2-3 have been scaled to match those from Channel 1. We label the strongest emission lines present, including PAH features.

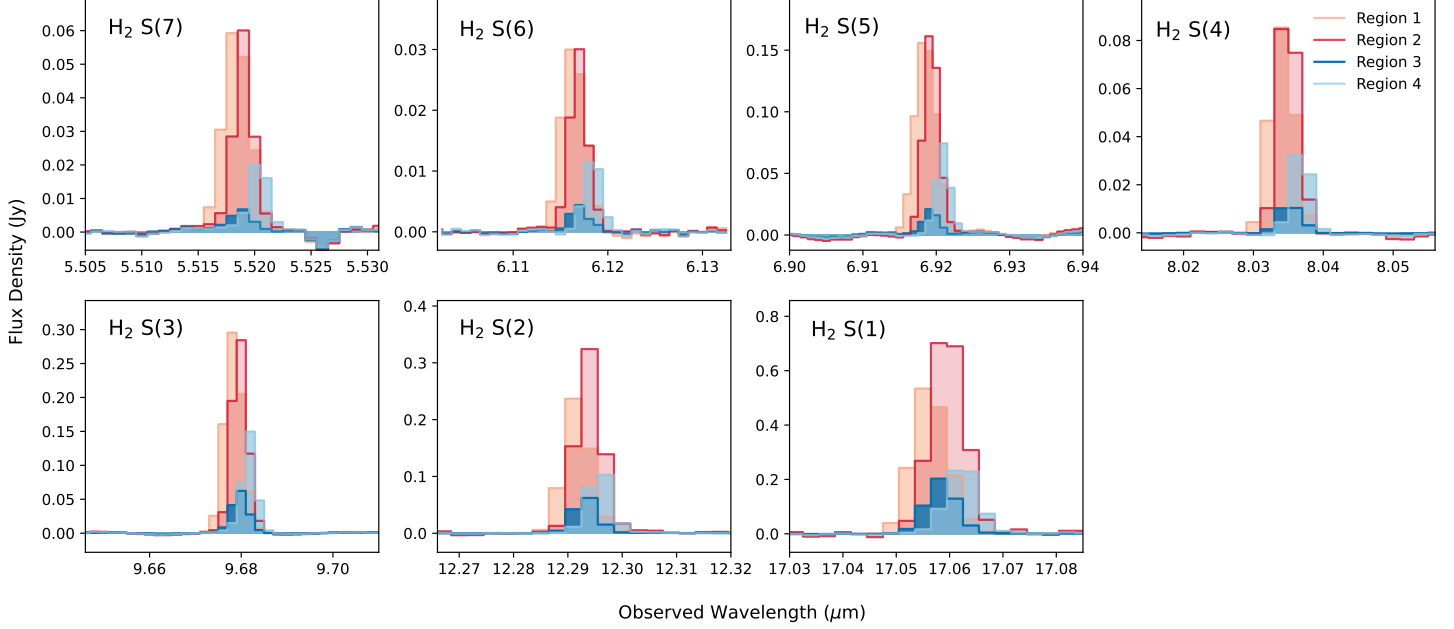


Figure 3. Foreground extinction-corrected continuum-subtracted H₂ emission for seven different transitions detected in four regions in the core of M83. The H₂ profiles are shown at the observed wavelengths.

Table 1. PAH emission line fluxes

Line	Rest Wavelength (μm)	Region 1	Region 2	Region 3	Region 4
		Flux ($10^{-16} \text{ W m}^{-2}$)			
PAH	6.22	43.30 ± 0.15	79.20 ± 0.17	16.40 ± 0.11	38.80 ± 0.13
PAH	7.42	34.40 ± 0.58	59.10 ± 0.52	4.03 ± 0.32	12.20 ± 0.41
PAH	7.60	59.90 ± 0.28	112.00 ± 0.30	25.50 ± 0.17	60.00 ± 0.22
PAH	7.85	63.50 ± 0.20	104.00 ± 0.24	24.70 ± 0.12	51.50 ± 0.17
PAH	8.61	34.50 ± 0.12	56.60 ± 0.13	14.00 ± 0.10	30.30 ± 0.91
PAH	11.33	29.50 ± 0.15	42.70 ± 0.15	10.50 ± 0.65	23.30 ± 0.92
PAH	12.62	25.50 ± 0.09	49.20 ± 0.15	9.69 ± 0.61	21.20 ± 0.95

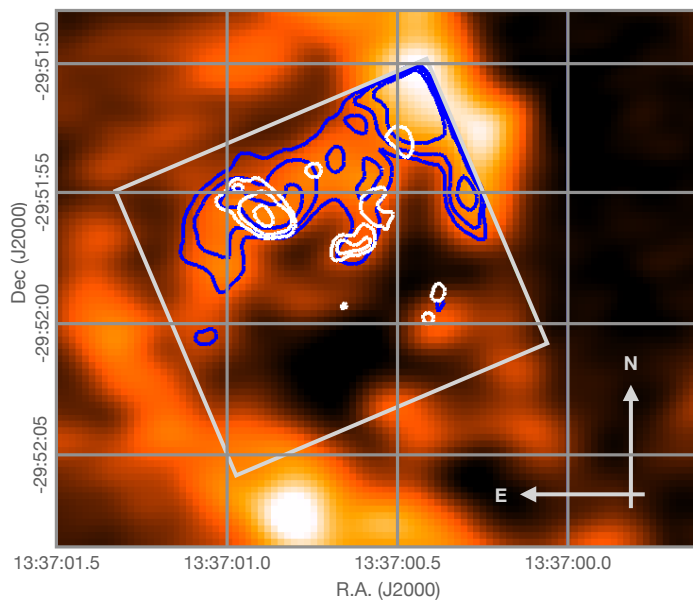


Figure 4. ^{12}CO (1–0) emission map of the nucleus of M83 by Hirota et al. (2018). The combined CO map has a resolution of $2.03'' \times 1.15''$. We show with a grey box the FoV of the combined MIRI/MRS channel-3 pointings. The blue contours show the concentrations of H_2 S(1) $17.035 \mu\text{m}$ emission, compared to the distribution of the much warmer H_2 from the S(7) $5.511 \mu\text{m}$ transition shown in white contours.

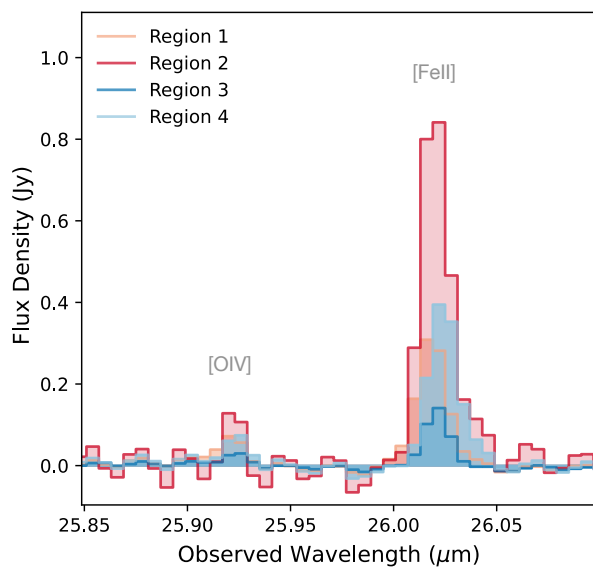


Figure 5. Continuum-subtracted [OIV] $25.89 \mu\text{m}$ and [FeII] $25.99 \mu\text{m}$ emission detected in all four regions in the core of M83.

Table 2. Mid-infrared emission line properties

Line Rest Wavelength (μm)	Region 1		Region 2		Region 3		Region 4	
	Flux ($10^{-18} W m^{-2}$)	FWHM (km s^{-1})	Flux ($10^{-18} W m^{-2}$)	FWHM (km s^{-1})	Flux ($10^{-18} W m^{-2}$)	FWHM (km s^{-1})	Flux ($10^{-18} W m^{-2}$)	FWHM (km s^{-1})
[ArII]	103.81 \pm 2.52	168 \pm 2	1454.70 \pm 61.92	125 \pm 2	44.98 \pm 2.38	145 \pm 4	315.85 \pm 1.74	130 \pm 3
Pfa	5.32 \pm 0.32	159 \pm 5	87.02 \pm 0.01	117 \pm 2	3.46 \pm 0.01	167 \pm 10	17.99 \pm 1.23	121 \pm 4
Hu β	2.08 \pm 0.27	173 \pm 14	23.36 \pm 3.70	120 \pm 10	1.53 \pm 0.25	280 \pm 29	6.81 \pm 1.09	163 \pm 14
[ArIII]	11.73 \pm 0.36	171 \pm 3	161.13 \pm 2.50	145 \pm 1	6.74 \pm 0.23	167 \pm 3	27.11 \pm 0.57	148 \pm 2
[SIV]	6.11 \pm 0.10	165 \pm 4	17.21 \pm 1.69	168 \pm 6	2.26 \pm 0.01	153 \pm 5	8.76 \pm 0.74	164 \pm 8
Hu α	2.32 \pm 0.22	152 \pm 8	25.76 \pm 1.52	138 \pm 4	0.99 \pm 0.07	128 \pm 5	6.53 \pm 0.51	153 \pm 6
[NeII]	308.49 \pm 5.39	179 \pm 1	3409.99 \pm 127.81	150 \pm 2	131.59 \pm 5.50	149 \pm 3	749.27 \pm 23.80	162 \pm 2
[NeV]	1.15 \pm 0.22	342 \pm 36	–	–	0.24 \pm 0.10	197 \pm 38	–	–
[CIII]	6.03 \pm 0.12	167 \pm 2	29.91 \pm 0.97	141 \pm 2	2.52 \pm 0.08	140 \pm 2	10.98 \pm 0.40	157 \pm 2
[NeIII]	72.13 \pm 1.16	199 \pm 2	153.19 \pm 2.01	199 \pm 2	30.93 \pm 0.39	175 \pm 2	168.91 \pm 2.70	199 \pm 2
[FeII]	9.24 \pm 2.09	260 \pm 33	26.25 \pm 18.50	235 \pm 113	3.56 \pm 0.71	220 \pm 24	14.98 \pm 5.03	254 \pm 50
[SIII]	125.98 \pm 1.04	186 \pm 1	1768.01 \pm 17.00	180 \pm 1	38.33 \pm 0.59	184 \pm 1	230.53 \pm 6.64	176 \pm 1
[FeIII]	9.72 \pm 0.69	202 \pm 8	93.90 \pm 4.81	195 \pm 5	3.99 \pm 0.40	206 \pm 11	26.51 \pm 1.41	192 \pm 5
[OIV]	5.11 \pm 1.18	182 \pm 25	6.26 \pm 5.37	112 \pm 82	1.98 \pm 0.60	150 \pm 27	4.62 \pm 1.74	146 \pm 33
[FeII]	25.90 \pm 2.20	197 \pm 9	69.73 \pm 6.25	191 \pm 9	9.88 \pm 0.96	165 \pm 9	32.58 \pm 2.73	196 \pm 9

4. DISCUSSION

4.1. Importance of warm H_2

The vast number of stars in the Universe formed primarily from molecular clouds, directly connecting SF to the surface density of molecular gas (e.g., Kennicutt 1998). Being such a critical ingredient of SF, it is essential to accurately measure and map the distribution of H_2 to fully understand the processes involved in forming stars, and how these evolve over cosmic history. Despite being the most abundant molecule in the universe, given the intrinsic nature of H_2 (being a weak rotational emitter), molecular hydrogen can be difficult to study directly. Instead, the next most abundant molecule, CO, is generally used as a molecular gas tracer in the local Universe (Leroy et al. 2011; Bolatto et al. 2013; Saintonge et al. 2017), as well as in intermediate-to-high redshift galaxies ($z \sim 1-2$, e.g., Tacconi et al. 2010; Pavese et al. 2018; Tacconi et al. 2020). A conversion factor (α_{CO}) is generally needed to measure the total molecular gas masses (e.g., Bolatto et al. 2013) as CO emission is consistently found to be optically thick. Recent evidence, indicates that α_{CO} varies substantially within and across galaxies at different epochs and metallicities (Sandstrom et al. 2013; Israel 2020).

Additional complications in measuring the total mass of H_2 involve scenarios where far-ultraviolet (FUV) photons permeate into molecular clouds photodissociating CO molecules, leaving a C^+ -emitting shell around the CO cloud (Madden et al. 2020). We note that the C^+ -emitting region is larger in those environments where the dust-to-gas ratio decreases and these FUV photons are able to permeate deeper into the cloud. This is in contrast to H_2 , which photodissociates via absorption of Lyman-Werner band photons, and can become self-shielded from photodissociating (Draine 2011; Krumholz 2013; Gnedin & Draine 2014), leaving a potentially significant reservoir of molecular hydrogen outside of the CO-emitting region. CO-dark molecular gas (Poglitsch et al. 1995; Madden et al. 1997; Grenier et al. 2005; Wolfire et al. 2010; Ackermann et al. 2012; Glover & Clark 2012a; Madden et al. 2020), as the name indicates, is not probed by CO, requiring other tracers to accurately quantify the total molecular gas mass,

$$M(\text{TOTAL})_{H_2} = M(\text{CO})_{H_2} + M(\text{CO} - \text{dark})_{H_2} \quad (1)$$

where $M(\text{TOTAL})_{H_2}$ is the total molecular gas mass, $M(\text{CO})_{H_2}$ is the molecular gas mass estimated using CO as a tracer of H_2 , and $M(\text{CO} - \text{dark})_{H_2}$ is the molecular gas mass contained in the warmer H_2 gas reservoir.

Star-forming galaxies (SFGs) typically have massive star clusters capable of photodissociating substantial fractions of CO molecules. Interestingly, theoretical

and observational studies have also shown that efficient SF is possible in these CO-dark regions, as well as in regions without H_2 , suggesting the existence of pathways to forming stars directly in the atomic ISM phase (Krumholz & Gnedin 2011; Glover & Clark 2012b; Kumari et al. 2020).

Adamo et al. (2015) have identified a relatively higher cluster formation efficiency in the nucleus of M83, compared to regions outside, which allows for a high enough production of energetic far-ultraviolet (FUV; $6 \text{ eV} < h\nu < 13.6 \text{ eV}$) photons capable of permeating the molecular clouds and photo-dissociating the CO gas. Given the findings by Adamo et al. (2015), studies such as that by Hernandez et al. (2021) have predicted the presence of large quantities of warm molecular gas (CO-dark gas) in the center of this spiral galaxy. The predictions by Hernandez et al. (2021) come from an observed excess in the column densities measured from the S II absorption localized to the nuclear regions, and absent on the disk of the galaxy. Hernandez et al. (2021) proposed that the observed S^+ excess is due to a significant fraction of the measured S II tracing the CO-dark (C^+ -emitting) gas along the line of sight, instead of only tracing the neutral gas. These new MIRI/MRS observations allow us to confirm such a prediction, as well as study the spatial distribution of this warm ($T \gtrsim 100 \text{ K}$) molecular gas compared to the much cooler ($\sim 10-20 \text{ K}$) ^{12}CO (1-0) gas.

The temperature equivalent of the upper energy level for the lowest pure rotational line transition, H_2 0-0 S(0) at $28.22\mu\text{m}$, is at 510 K. Togi & Smith (2016) note, however, that the Boltzmann distribution of energy levels can lead to excitation even at more conservative temperatures. Such a case might apply to the lowest transitions, S(0) to S(2), where these can be comfortably populated at excitation temperatures of $\sim 150 \text{ K}$, and even as low as $\sim 80 \text{ K}$. We detect seven H_2 transitions in all four regions of the M83 nucleus with varying strengths. In Figure 3 we show in different panels the H_2 profiles for each transition color-coded based on the specific region. Although we observe H_2 emission from all seven transitions throughout the core of the galaxy, the strongest emission is found in Regions 1 and 2, covering the northern-most areas, including the optical nucleus. Overall, the distribution of warm H_2 appears to weaken towards the southern regions of the nucleus, with Region 3 exhibiting the weakest H_2 emission.

In Figure 4 we show the cold molecular gas traced by the ^{12}CO (1-0) transition with the Atacama Large Millimeter/submillimeter Array (ALMA) as published by Hirota et al. (2018). Figure 4 provides a qualitative comparison between the CO emission and the distribu-

tion of H₂ gas for the S(1) and S(7) transitions in blue and white contours, respectively. The S(1) transition, expected to have the lowest excitation temperature out of all the detected transitions, appears to comfortably follow the cooler CO emission. The emission of the H₂ gas with the warmest temperatures, the S(7) transition, is primarily concentrated near the center of M83, covering an area with a diameter of ~ 60 pc.

We adopt the continuous-temperature model by Togi & Smith (2016) along with the measured H₂ fluxes to infer the molecular gas mass (no heavy element correction) in the different regions. Assuming the H₂ emission is optically thin, the H₂ excitation can be modeled through excitation diagrams relating the column density of the upper level of a particular transition (N_u) to its energy level (E_u), providing warm molecular gas masses by only varying the slope of the power law (n) and the lower temperature (T_l). Similar to the work by Togi & Smith (2016), we fixed the upper temperature (T_u) of the distribution to 2000 K, however, we highlight that we also tested setting this parameter free and confirmed that the fraction of the total warm molecular gas mass with $T_u > 2000$ K is negligible. In Table 3 we list the inferred foreground extinction-corrected fluxes for the detected transitions used in calculating the H₂ masses.

We show in columns 2 and 3 of Table 4 the two model-derived parameters, n and T_l , for all four nuclear regions studied here. We also include in Appendix A the excitation diagrams, along with the best fit models, for each region. The inferred power law indices range between 5.17 (in region 1 containing the optical nucleus) and 6.33. We note that in spite of the differences in spatial scales probed, these indices are within the range observed in the galaxy sample by Togi & Smith (2016), $3.79 < n < 6.39$. Generally, a steep power-law index (i.e., high values of n) imply low warm gas mass fractions; we highlight, however, that the work presented here with the application of the Togi & Smith (2016) model probes the smallest spatial scales (< 100 pc) to this day (see Armus et al. 2022 for a comparable study). Overall, our analysis shows relatively high T_l for all four regions, with the highest value observed in region 2. The high T_l in region 2, supports a scenario where the molecular gas has been recently heated by shocks (see Section 4.2).

Using the model-derived parameters listed in Table 4 we estimate warm ($T_l \gtrsim 250$ K) molecular gas masses of $3.34 \times 10^4 M_\odot$, $3.22 \times 10^4 M_\odot$, $8.76 \times 10^3 M_\odot$ and $1.32 \times 10^4 M_\odot$, for regions 1, 2, 3, and 4, respectively. Togi & Smith (2016) fitted continuous temperature distributions to a sample of SFGs with reliable molecular gas masses and calibrated an extrapolating temperature (50

K) providing a model that can be used to infer the total molecular gas mass directly from the H₂ rotational emission. Similar to the approach by Togi & Smith (2016), using the model-derived values we extrapolate the power law distribution to a temperature of 50 K to obtain an approximate value of the total molecular gas content accounting for the warm H₂ component. We list the estimated total molecular masses, $M(>50\text{K})_{\text{H}_2}$, in the fifth column in Table 4. Our inferred H₂ masses indicate that a large fraction of the total H₂ gas mass is found in the north-west region (region 2) $M(>50\text{K})_{\text{H}_2} = 40.3 \times 10^6 M_\odot$.

The H₂ masses listed in the the fifth column in Table 4 account for the molecular gas across a broad range of temperatures, including the warm component. Using the ¹²CO (1–0) intensity map shown in Figure 4 we integrate the line profiles for the same four MIRI/MRS regions studied here. For the nuclear regions in M83, Hirota et al. (2018) reports ¹²CO (1–0) peak temperatures between 10 and 20 K. Assuming a Galactic α_{CO} factor (Bolatto et al. 2013) we estimate total H₂ masses (probing the cold molecular gas) for all four regions and list them in the sixth column of Table 4 under $M(\text{CO})_{\text{H}_2}$. As noted above, studies have confirmed that the α_{CO} factor varies with metallicity. According to Bolatto et al. (2013), for a system with a metallicity similar to that measured for the nucleus of M83, $\log(Z/Z_\odot) \sim +0.2$ dex (Hernandez et al. 2021), the α_{CO} factor should be slightly lower than the Galactic value (we note, however, the large spread in the measurements), resulting in even lower $M(\text{CO})_{\text{H}_2}$ values than those listed in Table 4.

Comparing the total molecular gas masses inferred through the H₂ rotational lines, $M(>50\text{K})_{\text{H}_2}$, against those obtained using CO as a tracer of H₂, $M(\text{CO})_{\text{H}_2}$, we find that in all four regions the molecular gas masses accounting for the warm molecular component are higher than the $M(\text{CO})_{\text{H}_2}$ masses. These differences in masses can be attributed to the CO-dark component not probed by the CO emission. In the last column of Table 4 we list the difference between the two mass estimates, $M(>50\text{K})_{\text{H}_2} - M(\text{CO})_{\text{H}_2} = M(\text{CO-dark})$. The most extreme case appears to be observed in region 3, where $M(>50\text{K})_{\text{H}_2}$ is a factor of ~ 12 higher than $M(\text{CO})_{\text{H}_2}$. In this region we estimate that $\sim 92\%$ of the total molecular gas mass is contained in the warm (CO-dark) component. We highlight that the high CO-dark gas fraction observed in region 3 appears to be primarily driven by the low contents of CO (see Figure 4). For region 2 we estimate that $\sim 82\%$ of the total H₂ gas mass is not traced by the cold CO gas. Interestingly, the lowest fraction of CO-dark gas is found in region 1, which encapsulates the optical nucleus of this galaxy, with only $\sim 27\%$ of

the total H_2 gas mass found in the warm component. Lastly, we note that the molecular gas in region 2 accounts for $\sim 60\%$ of the total estimated H_2 gas mass of $67.90 (\pm 5.43) \times 10^6 M_\odot$ in the core of M83.

The spatially resolved study of the molecular gas content in the core of M83 presented here, began to confirm the predictions by Hernandez et al. (2021) where they propose that the high column densities of S II arise from a clumpy molecular gas environment with large quantities of CO-dark gas. The four pointings in Hernandez et al. (2021) exhibiting this excess of S II are located in regions 2 and 4 of the present study. Figure 4 highlights the clumpy nature of the warm molecular gas, particularly in these two regions. Furthermore, for the two specific regions where the excess of S II is observed, our study finds that 82% and 73% of the total H_2 gas mass (for regions 2 and 4, respectively) is contained in the warm molecular gas component.

Overall, this study highlights the importance of accounting for the warm molecular gas component when estimating total masses of the H_2 gas, specifically in regions of high SF. Our findings indicate that $\sim 75\%$ of the total molecular gas mass is contained in the warm component, when the fraction of CO-estimated H_2 mass, $M(\text{CO})_{\text{H}_2}$, is eliminated from the power-law derived mass estimates, $M(>50 \text{ K})_{\text{H}_2}$. Past studies have shown that the CO-dark gas can account for $>70\%$ of the total molecular gas, with the highest percentages found in low metallicity environments (Balashev et al. 2017; Madden et al. 2020; Lebouteiller & Ramambason 2022; Vizgan et al. 2022). Most recently, similar results were reported for the nearby dwarf galaxy WLM (with a metallicity of 13% solar) where Archer et al. (2022) find that 90% to 100% of the total molecular gas mass is contained in CO-dark H_2 clouds. Although outside of the scope of this work, future analysis of the MIRI/MRS observations will include a comparison of the H_2 emission maps with the ^{12}CO (1–0) intensity maps by Hirota et al. (2018) to discern the spatial differences between the warm and cold molecular gas.

4.2. $[\text{O IV}] 25.89\mu\text{m}$ emission and possible presence of shocks

Given that hot, massive stars emit a limited number of ionizing photons beyond the He^+ edge at 54 eV, the spectra of starburst sources are typically dominated by low-excitation emission lines. The excitation of high-ionization species, on the other hand, requires extreme conditions. These high-excitation species include the $[\text{O IV}] 25.89\mu\text{m}$ line with an ionization potential just above the He^+ edge. Surprisingly, past studies have detected this emission line in several different starbursts

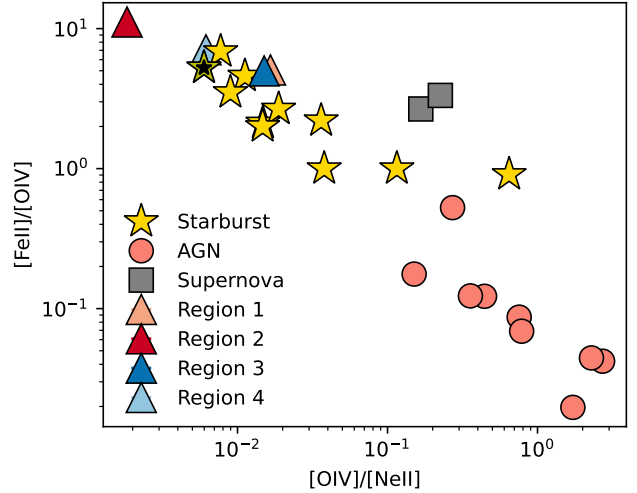


Figure 6. Fine-structure emission line ratios for the four different regions in the nucleus of M83 (shown in triangles). We compare these ratios with typical values obtained from sources with starburst-dominated (yellow stars from Verma et al. 2003), AGN-dominated (salmon circles from Sturm et al. 2002), and SNR (grey squares from Oliva et al. 1999a,b) emission.

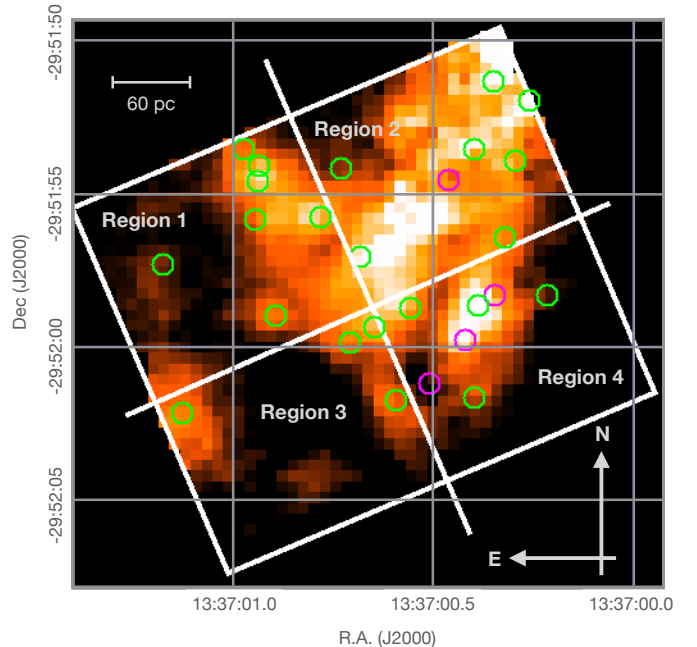


Figure 7. $[\text{FeII}]$ emission line map as observed by MIRI/MRS channel 4. We label the four different regions accordingly. We show with green apertures the location of supernovae remnants by Winkler et al. (2022). We display with magenta apertures the location of four young massive clusters studied in Hernandez et al. (2021).

Table 3. Measured H₂ fluxes

Line	Region 1	Region 2	Region 3	Region 4
	Flux ($10^{-18} \text{ W m}^{-2}$)			
H ₂ S(7)	17.30±0.93	9.42±1.13	1.66±0.76	5.01±0.47
H ₂ S(6)	8.07±0.20	5.57±0.15	0.92±0.12	2.38±0.14
H ₂ S(5)	36.99±0.92	31.32±2.07	3.91±0.64	9.95±0.38
H ₂ S(4)	18.32±3.06	19.13±4.34	2.50±0.17	5.45±3.36
H ₂ S(3)	74.27±0.26	31.24±0.27	7.05±0.11	2.11±0.16
H ₂ S(2)	29.66±0.41	38.06±0.02	7.36±0.24	12.47±0.42
H ₂ S(1)	49.60±0.58	60.38±1.62	13.35±0.14	20.72±0.35

Table 4. H₂ Model-derived parameters for the center of M83

Region	n	T_l (K)	$M(>T_l)_{\text{H}_2}$ (M_\odot)	$M(>50 \text{ K})_{\text{H}_2}$ (M_\odot)	$M(\text{CO})_{\text{H}_2}$ (M_\odot)	$M(\text{CO-dark})_{\text{H}_2}$ (M_\odot)
Region 1	5.17±0.04	252±3	$3.34 (\pm 0.13) \times 10^4$	$9.88 (\pm 0.46) \times 10^6$	7.22×10^6	2.65×10^6
Region 2	6.22±0.11	301±7	$3.22 (\pm 0.25) \times 10^4$	$40.3 (\pm 4.92) \times 10^6$	7.06×10^6	33.2×10^6
Region 3	6.33±0.18	269±9	$8.76 (\pm 0.82) \times 10^3$	$10.0 (\pm 2.00) \times 10^6$	0.80×10^6	9.22×10^6
Region 4	5.70±0.11	267±9	$1.32 (\pm 0.14) \times 10^4$	$7.72 (\pm 1.03) \times 10^6$	2.07×10^6	5.65×10^6
Total			$8.76 (\pm 0.33) \times 10^4$	$67.90 (\pm 5.43) \times 10^6$	17.15×10^6	50.74×10^6

(e.g., Lutz et al. 1998; Verma et al. 2003; Hao et al. 2009; Bernard-Salas et al. 2009). For many of these objects, the [O IV] detection cannot be attributed to an enshrouded AGN; instead the mechanism believed to be responsible for the production of these highly ionizing photons ($\gtrsim 54$ eV) is very hot stars (e.g., Wolf-Rayet stars), ionizing shocks (Lutz et al. 1998), and although debated, most recently it was suggested that high-mass X-ray binaries could also be responsible for these photons (Schaerer et al. 2019; Senchyna et al. 2020). We note that no AGN has been identified in M83, and even the possible presence of a massive black hole is debated (cf. Russell et al. 2020, Appendix A2). However, some hard X-ray point sources are seen (at least in projection) toward the nuclear region (Long et al. 2014; Russell et al. 2020).

In Figure 5 we show the emission profiles of [O IV] 25.89 μm and [Fe II] 25.99 μm . Due to the strong H₂ emission discussed in the previous section, it is conceivable that ionizing shocks are indeed contributing to the observed [O IV] emission. One way to explore the possible shock contributions in these active environments is to compare the strength of the [O IV] feature to the emission from other fine-structure lines expected to be strong in partially ionized regions with shocks.

Since Fe is known to strongly deplete onto grains in the ISM (Savage & Sembach 1996), the shock destruction of dust grains typically boosts the [Fe II] emission

(already present in ionized zones). The [Fe II]/[O IV] ratio along with the [O IV]/[Ne II] fluxes are typically used to distinguish between excitations driven by starbursts, AGN or supernova remnant shocks (e.g., Lutz et al. 2003; Sturm et al. 2006; Inami et al. 2013). In Figure 6 we show the fine-structure emission line ratios from starburst-dominated systems measured by Verma et al. (2003) as yellow stars, along with the ratios inferred for AGN-dominated emission by Sturm et al. (2002) as salmon-colored circles, and line ratios from supernova remnants in grey squares (Oliva et al. 1999a,b). Both starburst-dominated systems and supernova remnant shocks tend to show much weaker [O IV] emission (e.g., higher [Fe II]/[O IV] ratios), compared to those from AGNs, therefore occupying the top half of Figure 6.

The [O IV] emission from the nuclear starburst in M83 was previously detected in observations taken with ISO Short Wavelength Spectrometer (ISO-SWS) and reported by Verma et al. (2003), marked with a black star in Figure 6. We also include in Figure 6 the inferred ratios for the four pre-defined regions in the core of M83, shown as triangles. We highlight that the fine-structure emission line ratios reported by Verma et al. (2003) for M83 are in essence the integrated fluxes for all of the four regions in this study. From Figure 6 it is clear that all four regions in the core of M83 have comparable ratios to those characteristic of starburst systems with varia-

tions from region to region, and similarly weak [O IV] emission to those detected in supernova remnant shocks.

Due to the nature of iron, as detailed earlier, previous studies have extensively used the near-infrared [Fe II] emission in starburst galaxies to identify new supernova remnants (SNRs; e.g., Labrie & Pritchett 2006). Furthermore, according to Blair et al. (2014) and Winkler et al. (2022), a number of the known SNRs in M83 have indeed been identified as strong [Fe II] emitters. We show in Figure 7 the [Fe II] emission at $25.99 \mu\text{m}$. To investigate if the [Fe II] emission displays any structure coincident with SNRs, we highlight in Figure 7 with green apertures the location of SNRs most recently identified in the nuclear region by Winkler et al. (2022), many of which are isolated [Fe II] sources. The [Fe II] emission appears to be diffuse and mostly concentrated in region 2, extending into regions 1 and 4. Most of the SNRs are coincident with the region of bright diffuse [Fe II] emission, but enhanced emission from the individual SNRs is not generally apparent.

Studies such as that by Labrie & Pritchett (2006) have reported [Fe II] emission with a spatially-extended component in several nearby starburst galaxies, where the SNR [Fe II] emission does indeed account for $\sim 10\%$ of the total [Fe II] luminosity. We also show in Figure 7 with magenta apertures the location of four young massive clusters studied in Hernandez et al. (2021) with ages ranging from ~ 3 to 10 Myr (Wofford et al. 2011; Hernandez et al. 2019). Two of these clusters appear to bracket a region with observed strong [Fe II] emission while two others do not have a strong association, making an attribution unclear.

As mentioned before, the nucleus of M83 has been studied extensively at different wavelengths. For example, recently Russell et al. (2020) presented a detailed discussion of the multiwavelength characteristics of the nucleus (their Section 4.5 and Figure 11). Similarly, Long et al. (2014) have carefully studied the X-ray emission in the nucleus of M83. These authors highlight that the soft X-ray emission ($0.35\text{-}1.1$ keV) in the nuclear region of the galaxy has a clumpy and diffuse nature, while the hard X-ray emission ($2.6\text{-}8.0$ keV) is dominated by point sources which are primarily high mass X-ray binaries. The soft X-ray emission in the nuclear region, they propose, is energized by both the SNR population and the strong stellar winds from all the young massive stars. In Figure 8 we compare the Fe II emission contours detected in the MIRI observations, to the soft and hard X-ray emission maps by Long et al. (2014). Overall, the observed diffuse soft X-ray emission is comparable in nature to the [Fe II] emission, this in contrast to the point-source emission from hard X-rays. Interestingly, Zhang

(2018) reviews the nature of galactic winds and stellar feedback from starbursts and describes a scenario where the starburst region launches a hot wind that expands outward. As this hot wind encounters the surrounding large-scale ISM, shock waves produce structured soft X-ray emission. Under this scenario the observed clumpy and diffuse soft X-ray emission, as well as the similarly diffuse [Fe II] emission, could be tracing the shocks from such an interaction.

Both photoionization and shocks can in principle excite gas in starburst systems. Assuming a scenario similar to that described in Zhang (2018), we can explore the properties of the expected shocks. In Figure 9 we show the [S IV]/[Ne II] versus [Ne III]/[Ne II] emission line diagnostic diagram and overlay the shock ionization model grids of Allen et al. (2008), with magnetic field strengths ranging from 0.1 to $100 \mu\text{G}$ and shock speeds of 100 to 200 km s^{-1} . According to these shock ionization models and assuming shocks are the main ionization mechanism in these intense environments, the shocks observed in regions 1, 3 and 4 display speeds of $\lesssim 150 \text{ km s}^{-1}$, whereas the shock speeds observed in region 2 is $> 150 \text{ km s}^{-1}$. Additionally, these models indicate that the strength of the magnetic fields is similar in regions 1, 3 and 4 ($\sim 20 \mu\text{G}$), and higher in these regions than in region 2 ($\ll 0.1 \mu\text{G}$). For completion, we also include in Figure 9 the line ratios of starburst-, AGN- and supernova-dominated emission. We note that for a fraction of the objects in the starburst-dominated sample, the observed ratios agree with the shock ionization model by Allen et al. (2008). We stress that while the emission line ratios measured in the different nuclear regions in M83 are consistent with values expected from shock ionization, comparing to photoionization models by Levesque et al. (2010) we confirmed that young starbursts with ages ~ 3 Myr, above-solar metallicity and ionization parameter of $2 \times 10^7 \text{ cm s}^{-1}$ can similarly reproduce the measured flux ratios. A similar trend is observed for the fraction of objects in the starburst-dominated sample that agree with the shock ionization models; these ratios can also be reproduced by a young starburst. Definitive confirmation of a shock-dominated environment in the nucleus of M83 will require self-consistent modeling of the ionization by shocks and massive stars, a task that will be explored in future studies.

5. SUMMARY

We present the first analysis of the recently-acquired JWST MIRI/MRS observations of the nucleus of M83, covering a region of $\sim 200 \text{ pc} \times 200 \text{ pc}$. The spectroscopic observations exhibit a plethora of emission features characterizing the multi-phase ISM and its differ-

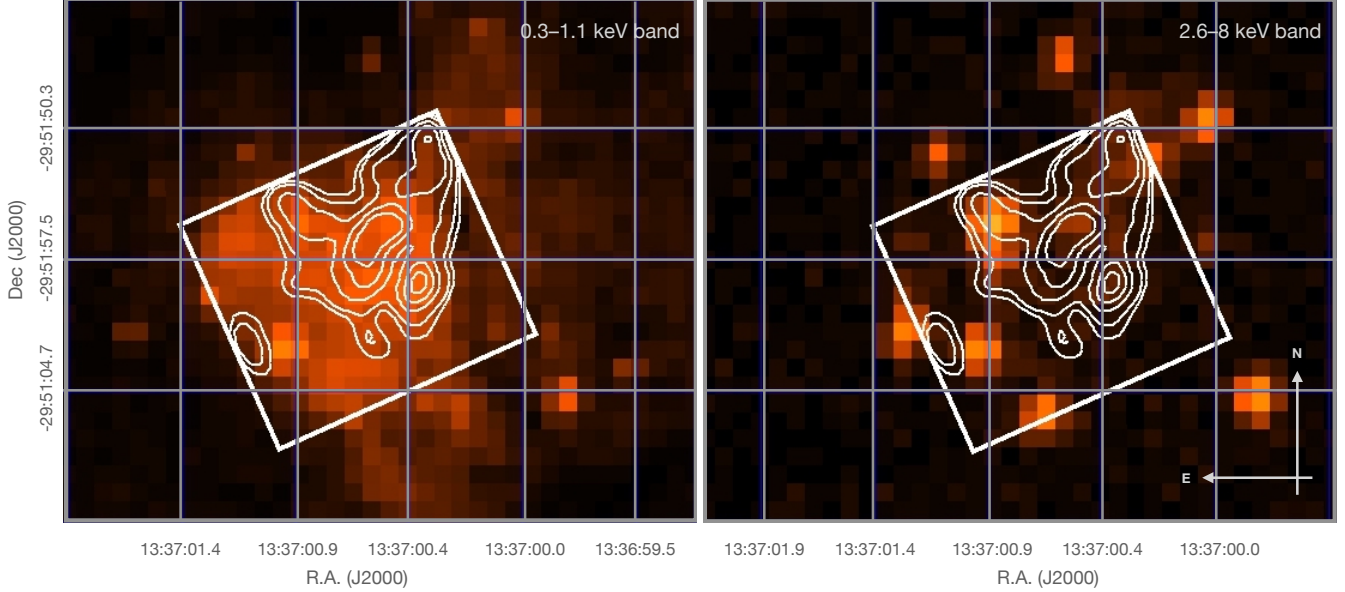


Figure 8. In both panels we show the [Fe II] 25.99 μm emission contours in white, along with the MIRI/MRS channel 4 FoV for context. *Left:* Chandra image in the 0.3-1.1 keV band by Long et al. (2014). *Right:* Chandra image in the 2.6-8 keV band by Long et al. (2014).

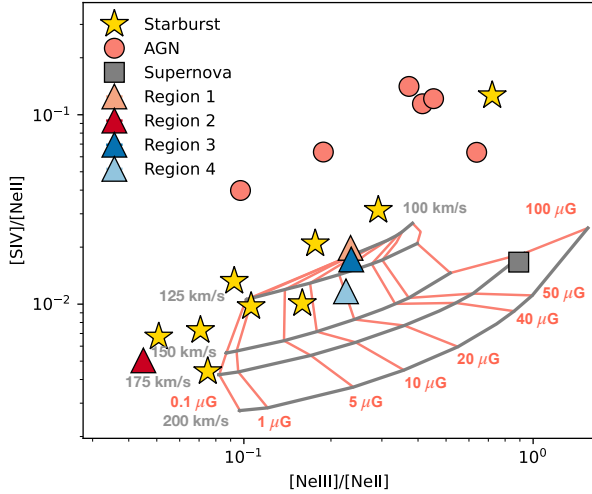


Figure 9. [SIV]/[NeII] vs. [NeIII]/[NeII] emission line diagnostic diagram. The ratios for the different regions are shown with triangles of different colors. We show in grey the shock speeds and in salmon the magnetic field strengths according to the shock ionization model grid by Allen et al. (2008). For completion, we also include the typical values from sources with starburst-dominated (yellow stars from Verma et al. 2003), AGN-dominated (salmon circles from Sturm et al. 2002), and SNR (grey squares from Oliva et al. 1999a,b) emission.

ent components: ionized gas, warm molecular gas, and dust. We summarize our findings as follows:

- Assuming a uniform power law model as proposed by Togi & Smith (2016), we estimate for

the first time molecular gas masses accounting for the warm H_2 gas component in four regions in the core of M83 obtaining values of $9.88 \times 10^6 M_\odot$, $40.3 \times 10^6 M_\odot$, $10.0 \times 10^6 M_\odot$ and $7.72 \times 10^6 M_\odot$, for regions 1, 2, 3, and 4, respectively.

- We report on the molecular gas masses as traced by the ^{12}CO (1–0) transition spatially coincident with the four MIRI/MRS regions in the nucleus of M83. We find that in regions 2, 3 and 4, the CO-dark gas accounts for $>70\%$ of their total molecular gas masses.
- We find that the total molecular gas mass accounting for the warm H_2 component inferred in region 3 (south of the optical nucleus) is a factor of ~ 12 higher than the mass inferred through the CO emission. This difference in molecular gas masses appears to be driven by a localized lack of cold molecular gas emission as traced by the ^{12}CO (1–0) transition.
- Our findings indicate that $\sim 75\%$ of the total molecular gas mass is contained in the warm H_2 component.
- We detect emission from the high-excitation species [OIV] 25.89 μm in the core of M83 and report varying emission strengths in all four regions.
- We compare the [FeII] 25.99 μm emission map to the location of SNRs (Winkler et al. 2022) and a

few massive stellar clusters (Hernandez et al. 2021) and find no correlation between the [Fe II] emission and the location of these sources. We instead observe clumpy and diffuse [FeII] 25.99 μm emission, comparable to the soft X-Ray emission detected in the nucleus of this galaxy by Long et al. (2014).

- We propose that the diffused [Fe II] 25.99 μm emission might be tracing shocks created during the interactions between the hot wind produced by the starburst and the much cooler ISM above the galactic plane, similar to the model described in Zhang (2018). Confirmation of this scenario requires self-consistent photoionization and shock modeling.

The initial study presented here shows the incredible power and bright future of this new mid-infrared instrument and configuration, MIRI/MRS. We highlight that we will further exploit these MRS observations focusing on spatially-resolved studies of the physical and chemical properties of the multi-phase ISM in the nuclear region of M83 (Jones et al. in prep.). The spectroscopic capabilities and unprecedented mid-infrared sensitivity of MIRI are allowing us to better understand the intense environments of these nearby starburst galaxies,

in many cases comparable to those expected in the very first galaxies.

We are grateful to Akihiko Hirota for sharing their calibrated Atacama Large Millimeter/submillimeter Array (ALMA) CO emission map. This work is based on observations made with the NASA/ESA/CSA *James Webb Space Telescope*. Support for program JWST-GO-02291 was provided by NASA through a grant from the Space Telescope Science Institute, which is operated by the Associations of Universities for Research in Astronomy, Incorporated, under NASA contract NAS5-26555. This work is based on observations made with the NASA/ESA/CSA James Webb Space Telescope. The data were obtained from the Mikulski Archive for Space Telescopes at the Space Telescope Science Institute, which is operated by the Association of Universities for Research in Astronomy, Inc., under NASA contract NAS 5-03127 for JWST. These observations are associated with program #02219.

Facilities: JWST(MIRI)

Software: dust_extinction (Gordon et al. 2021)

APPENDIX

A. APPENDIX INFORMATION

The H_2 gas masses were inferred adopting the approach by Togi & Smith (2016). We modeled the H_2 excitation and obtained warm H_2 gas masses ($M(>T_l)_{\text{H}_2}$; fourth column in Table 4), by varying the power-law slope and T_l . In Figure 10 we show the excitation diagrams for the different regions in the nucleus of M83. As noted by Donnan et al. (2023), the S(3) transition at 9.665 μm is found at the peak of the silicate absorption, and therefore highly sensitive to extinction. In the analysis by Donnan et al. (2023), they include this line with high uncertainties to ensure it does not bias their H_2 excitation model fits. For our analysis, we exclude the S(3) transitions for Regions 2, 3 and 4, as they appear to strongly bias the model fits, indicating high degrees of extinction. Overall, the best model fits accurately characterize the observed column densities.

As detailed in Section 4.1, the inferred models recover the total molecular gas mass, $M(>50 \text{ K})_{\text{H}_2}$, by extrapolating the fitted power-law temperature distributions to the calibrated single lower cutoff temperature (50 K; Togi & Smith 2016).

REFERENCES

- Ackermann, M., Ajello, M., Allafort, A., et al. 2012, *A&A*, 538, A71, doi: [10.1051/0004-6361/201117539](https://doi.org/10.1051/0004-6361/201117539)
- Adamo, A., Kruijssen, J. M. D., Bastian, N., Silva-Villa, E., & Ryon, J. 2015, *MNRAS*, 452, 246, doi: [10.1093/mnras/stv1203](https://doi.org/10.1093/mnras/stv1203)
- Adamo, A., Östlin, G., Zackrisson, E., et al. 2010, *MNRAS*, 407, 870, doi: [10.1111/j.1365-2966.2010.16983.x](https://doi.org/10.1111/j.1365-2966.2010.16983.x)
- Allen, M. G., Groves, B. A., Dopita, M. A., Sutherland, R. S., & Kewley, L. J. 2008, *ApJS*, 178, 20, doi: [10.1086/589652](https://doi.org/10.1086/589652)
- Annibali, F., & Tosi, M. 2022, *Nature Astronomy*, 6, 48, doi: [10.1038/s41550-021-01575-x](https://doi.org/10.1038/s41550-021-01575-x)
- Appleton, P. N., Xu, K. C., Reach, W., et al. 2006, *ApJL*, 639, L51, doi: [10.1086/502646](https://doi.org/10.1086/502646)

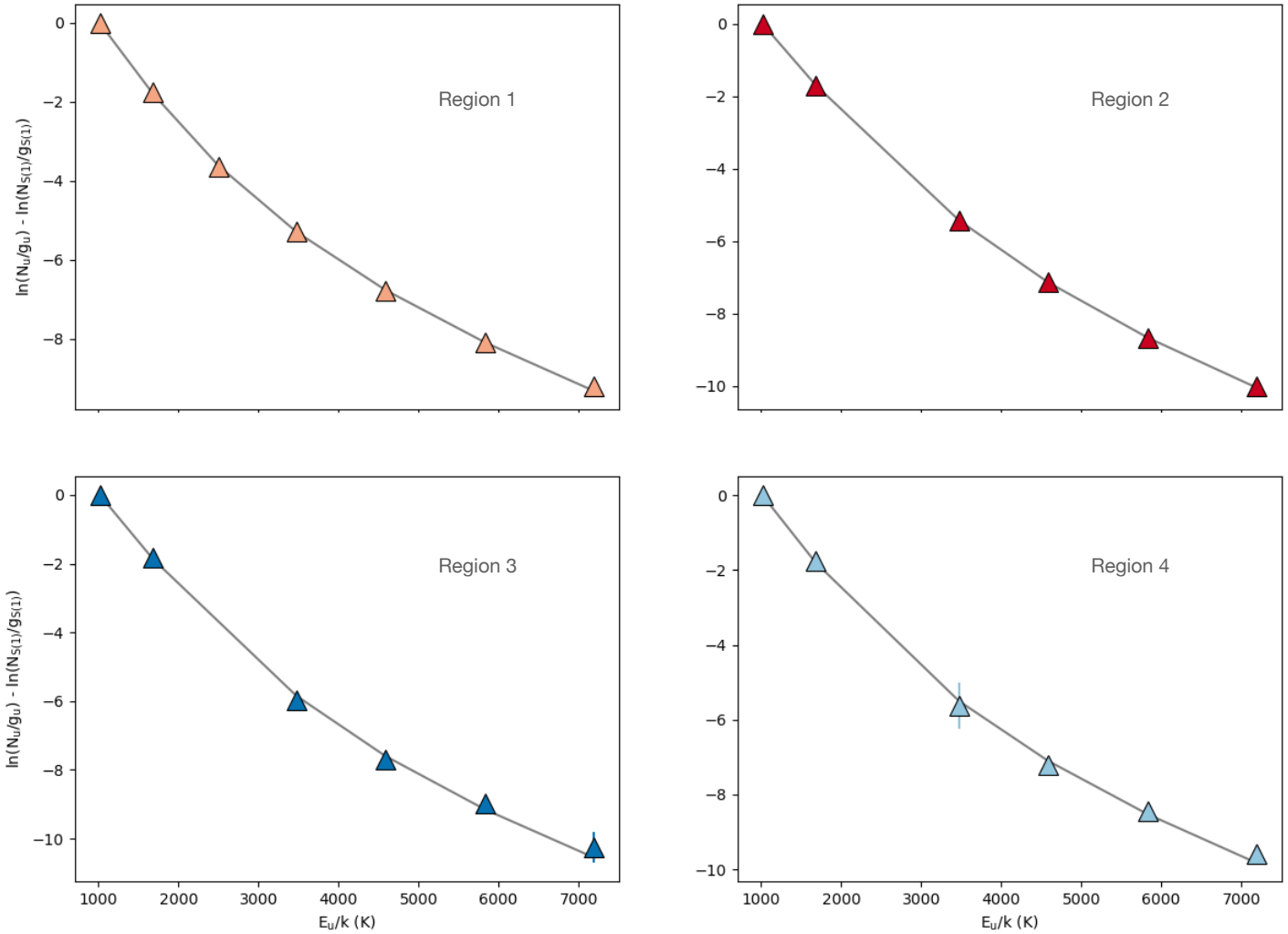


Figure 10. Excitation diagrams for all four M83 nuclear regions. Similar to the work by Togi & Smith (2016) the N_u/g_u ratios are normalized to the S(1) transition. We show with a grey line the best model fit adopting the parameters listed in Table 4.

Archer, H. N., Hunter, D. A., Elmegreen, B. G., et al. 2022, *AJ*, 163, 141, doi: [10.3847/1538-3881/ac4e88](https://doi.org/10.3847/1538-3881/ac4e88)

Armus, L., Charmandaris, V., & Soifer, B. T. 2020, *Nature Astronomy*, 4, 467, doi: [10.1038/s41550-020-1106-3](https://doi.org/10.1038/s41550-020-1106-3)

Armus, L., Charmandaris, V., Spoon, H. W. W., et al. 2004, *ApJS*, 154, 178, doi: [10.1086/422915](https://doi.org/10.1086/422915)

Armus, L., Bernard-Salas, J., Spoon, H. W. W., et al. 2006, *ApJ*, 640, 204, doi: [10.1086/500040](https://doi.org/10.1086/500040)

Armus, L., Charmandaris, V., Bernard-Salas, J., et al. 2007, *ApJ*, 656, 148, doi: [10.1086/510107](https://doi.org/10.1086/510107)

Armus, L., Lai, T., U, V., et al. 2022, arXiv e-prints, arXiv:2209.13125. <https://arxiv.org/abs/2209.13125>

Balashov, S. A., Noterdaeme, P., Rahmani, H., et al. 2017, *MNRAS*, 470, 2890, doi: [10.1093/mnras/stx1339](https://doi.org/10.1093/mnras/stx1339)

Balzano, V. A. 1983, *ApJ*, 268, 602, doi: [10.1086/160983](https://doi.org/10.1086/160983)

Bernard-Salas, J., Spoon, H. W. W., Charmandaris, V., et al. 2009, *ApJS*, 184, 230, doi: [10.1088/0067-0049/184/2/230](https://doi.org/10.1088/0067-0049/184/2/230)

Blair, W. P., Chandar, R., Dopita, M. A., et al. 2014, *ApJ*, 788, 55, doi: [10.1088/0004-637X/788/1/55](https://doi.org/10.1088/0004-637X/788/1/55)

Bolatto, A. D., Wolfire, M., & Leroy, A. K. 2013, *ARA&A*, 51, 207, doi: [10.1146/annurev-astro-082812-140944](https://doi.org/10.1146/annurev-astro-082812-140944)

Brandl, B. R., Bernard-Salas, J., Spoon, H. W. W., et al. 2006, *ApJ*, 653, 1129, doi: [10.1086/508849](https://doi.org/10.1086/508849)

Bresolin, F., & Kennicutt, Robert C., J. 2002, *ApJ*, 572, 838, doi: [10.1086/340371](https://doi.org/10.1086/340371)

Bresolin, F., Kudritzki, R.-P., Urbaneja, M. A., et al. 2016, *ApJ*, 830, 64, doi: [10.3847/0004-637X/830/2/64](https://doi.org/10.3847/0004-637X/830/2/64)

Bruzzeese, S. M., Thilker, D. A., Meurer, G. R., et al. 2020, *MNRAS*, 491, 2366, doi: [10.1093/mnras/stz3151](https://doi.org/10.1093/mnras/stz3151)

- Cairós, L. M., González-Pérez, J. N., Weilbacher, P. M., & Manso Sainz, R. 2022, *A&A*, 664, A144, doi: [10.1051/0004-6361/202243028](https://doi.org/10.1051/0004-6361/202243028)
- Callanan, D., Longmore, S. N., Kruijssen, J. M. D., et al. 2021, *MNRAS*, 505, 4310, doi: [10.1093/mnras/stab1527](https://doi.org/10.1093/mnras/stab1527)
- Díaz, R. J., Dottori, H., Agüero, M. P., et al. 2006, *ApJ*, 652, 1122, doi: [10.1086/507886](https://doi.org/10.1086/507886)
- Donnan, F. R., García-Bernete, I., Rigopoulou, D., et al. 2023, *MNRAS*, 519, 3691, doi: [10.1093/mnras/stac3729](https://doi.org/10.1093/mnras/stac3729)
- Dopita, M. A., Blair, W. P., Long, K. S., et al. 2010, *ApJ*, 710, 964, doi: [10.1088/0004-637X/710/2/964](https://doi.org/10.1088/0004-637X/710/2/964)
- Draine, B. T. 2011, *Physics of the Interstellar and Intergalactic Medium*
- Ducci, L., Sasaki, M., Haberl, F., & Pietsch, W. 2013, *A&A*, 553, A7, doi: [10.1051/0004-6361/201321035](https://doi.org/10.1051/0004-6361/201321035)
- Elmegreen, D. M., Chromey, F. R., & Warren, A. R. 1998, *AJ*, 116, 2834, doi: [10.1086/300657](https://doi.org/10.1086/300657)
- Finkelstein, S. L., D'Aloisio, A., Paardekooper, J.-P., et al. 2019, *ApJ*, 879, 36, doi: [10.3847/1538-4357/ab1ea8](https://doi.org/10.3847/1538-4357/ab1ea8)
- Flury, S. R., Jaskot, A. E., Ferguson, H. C., et al. 2022a, *ApJS*, 260, 1, doi: [10.3847/1538-4365/ac5331](https://doi.org/10.3847/1538-4365/ac5331)
- . 2022b, *ApJ*, 930, 126, doi: [10.3847/1538-4357/ac61e4](https://doi.org/10.3847/1538-4357/ac61e4)
- Genzel, R., & Cesarsky, C. J. 2000, *ARA&A*, 38, 761, doi: [10.1146/annurev.astro.38.1.761](https://doi.org/10.1146/annurev.astro.38.1.761)
- Glover, S. C. O., & Clark, P. C. 2012a, *MNRAS*, 426, 377, doi: [10.1111/j.1365-2966.2012.21737.x](https://doi.org/10.1111/j.1365-2966.2012.21737.x)
- . 2012b, *MNRAS*, 421, 9, doi: [10.1111/j.1365-2966.2011.19648.x](https://doi.org/10.1111/j.1365-2966.2011.19648.x)
- Gnedin, N. Y., & Draine, B. T. 2014, *ApJ*, 795, 37, doi: [10.1088/0004-637X/795/1/37](https://doi.org/10.1088/0004-637X/795/1/37)
- Gordon, K. D., Misselt, K. A., Bouwman, J., et al. 2021, *ApJ*, 916, 33, doi: [10.3847/1538-4357/ac00b7](https://doi.org/10.3847/1538-4357/ac00b7)
- Grenier, I. A., Casandjian, J.-M., & Terrier, R. 2005, *Science*, 307, 1292, doi: [10.1126/science.1106924](https://doi.org/10.1126/science.1106924)
- Hao, L., Wu, Y., Charmandaris, V., et al. 2009, *ApJ*, 704, 1159, doi: [10.1088/0004-637X/704/2/1159](https://doi.org/10.1088/0004-637X/704/2/1159)
- Heckman, T. M. 1994, in *Mass-Transfer Induced Activity in Galaxies*, ed. I. Shlosman, 234
- Heckman, T. M. 1998, in *Astronomical Society of the Pacific Conference Series*, Vol. 148, *Origins*, ed. C. E. Woodward, J. M. Shull, & J. Thronson, Harley A., 127. <https://arxiv.org/abs/astro-ph/9708263>
- Heckman, T. M., Armus, L., & Miley, G. K. 1990, *ApJS*, 74, 833, doi: [10.1086/191522](https://doi.org/10.1086/191522)
- Heckman, T. M., Borthakur, S., Overzier, R., et al. 2011, *ApJ*, 730, 5, doi: [10.1088/0004-637X/730/1/5](https://doi.org/10.1088/0004-637X/730/1/5)
- Hernandez, S., Larsen, S., Aloisi, A., et al. 2019, *ApJ*, 872, 116, doi: [10.3847/1538-4357/ab017a](https://doi.org/10.3847/1538-4357/ab017a)
- Hernandez, S., Aloisi, A., James, B. L., et al. 2021, *ApJ*, 908, 226, doi: [10.3847/1538-4357/abd6c4](https://doi.org/10.3847/1538-4357/abd6c4)
- Hirota, A., Egusa, F., Baba, J., et al. 2018, *PASJ*, 70, 73, doi: [10.1093/pasj/psy071](https://doi.org/10.1093/pasj/psy071)
- Ho, L. C., & Filippenko, A. V. 1996, *ApJ*, 472, 600, doi: [10.1086/178091](https://doi.org/10.1086/178091)
- Houck, J. R., Roellig, T. L., van Cleve, J., et al. 2004, *ApJS*, 154, 18, doi: [10.1086/423134](https://doi.org/10.1086/423134)
- Houghton, R. C. W., & Thatte, N. 2008, *MNRAS*, 385, 1110, doi: [10.1111/j.1365-2966.2008.12893.x](https://doi.org/10.1111/j.1365-2966.2008.12893.x)
- Hunt, Q., Gallo, E., Chandar, R., et al. 2021, *ApJ*, 912, 31, doi: [10.3847/1538-4357/abe531](https://doi.org/10.3847/1538-4357/abe531)
- Inami, H., Armus, L., Charmandaris, V., et al. 2013, *ApJ*, 777, 156, doi: [10.1088/0004-637X/777/2/156](https://doi.org/10.1088/0004-637X/777/2/156)
- Israel, F. P. 2020, *A&A*, 635, A131, doi: [10.1051/0004-6361/201834198](https://doi.org/10.1051/0004-6361/201834198)
- Izotov, Y. I., Guseva, N. G., Fricke, K. J., et al. 2021, *A&A*, 646, A138, doi: [10.1051/0004-6361/202039772](https://doi.org/10.1051/0004-6361/202039772)
- Izotov, Y. I., Schaerer, D., Worseck, G., et al. 2018a, *MNRAS*, 474, 4514, doi: [10.1093/mnras/stx3115](https://doi.org/10.1093/mnras/stx3115)
- Izotov, Y. I., Worseck, G., Schaerer, D., et al. 2018b, *MNRAS*, 478, 4851, doi: [10.1093/mnras/sty1378](https://doi.org/10.1093/mnras/sty1378)
- James, B. L., Aloisi, A., Heckman, T., Sohn, S. T., & Wolfe, M. A. 2014, *ApJ*, 795, 109, doi: [10.1088/0004-637X/795/2/109](https://doi.org/10.1088/0004-637X/795/2/109)
- Kennicutt, Robert C., J. 1998, *ApJ*, 498, 541, doi: [10.1086/305588](https://doi.org/10.1086/305588)
- Kim, H., Whitmore, B. C., Chandar, R., et al. 2012, *ApJ*, 753, 26, doi: [10.1088/0004-637X/753/1/26](https://doi.org/10.1088/0004-637X/753/1/26)
- Knapen, J. H. 2004, in *Astrophysics and Space Science Library*, Vol. 319, *Penetrating Bars Through Masks of Cosmic Dust*, ed. D. L. Block, I. Puerari, K. C. Freeman, R. Groess, & E. K. Block, 189, doi: [10.1007/978-1-4020-2862-5_16](https://doi.org/10.1007/978-1-4020-2862-5_16)
- Knapen, J. H., Sharp, R. G., Ryder, S. D., et al. 2010, *MNRAS*, 408, 797, doi: [10.1111/j.1365-2966.2010.17180.x](https://doi.org/10.1111/j.1365-2966.2010.17180.x)
- Krumholz, M. R. 2013, *MNRAS*, 436, 2747, doi: [10.1093/mnras/stt1780](https://doi.org/10.1093/mnras/stt1780)
- Krumholz, M. R., & Gnedin, N. Y. 2011, *ApJ*, 729, 36, doi: [10.1088/0004-637X/729/1/36](https://doi.org/10.1088/0004-637X/729/1/36)
- Kumari, N., Irwin, M. J., & James, B. L. 2020, *A&A*, 634, A24, doi: [10.1051/0004-6361/201732467](https://doi.org/10.1051/0004-6361/201732467)
- Labiano, A., Argyriou, I., Álvarez-Márquez, J., et al. 2021, *A&A*, 656, A57, doi: [10.1051/0004-6361/202140614](https://doi.org/10.1051/0004-6361/202140614)
- Labrie, K., & Pritchett, C. J. 2006, *Near-Infrared [Fe II] Emission in Starburst Galaxies. I. Measured Properties*, doi: [10.1086/505579](https://doi.org/10.1086/505579)
- Lahuis, F., Spoon, H. W. W., Tielens, A. G. G. M., et al. 2007, *ApJ*, 659, 296, doi: [10.1086/512050](https://doi.org/10.1086/512050)
- Le Floch, E., Papovich, C., Dole, H., et al. 2005, *ApJ*, 632, 169, doi: [10.1086/432789](https://doi.org/10.1086/432789)

- Lebouteiller, V., & Ramambason, L. 2022, *A&A*, 667, A34, doi: [10.1051/0004-6361/202243865](https://doi.org/10.1051/0004-6361/202243865)
- Leitherer, C., Ferguson, H. C., Heckman, T. M., & Lowenthal, J. D. 1995, *ApJL*, 454, L19, doi: [10.1086/309760](https://doi.org/10.1086/309760)
- Leitherer, C., & Heckman, T. M. 1995, *ApJS*, 96, 9, doi: [10.1086/192112](https://doi.org/10.1086/192112)
- Leroy, A. K., Bolatto, A., Gordon, K., et al. 2011, *ApJ*, 737, 12, doi: [10.1088/0004-637X/737/1/12](https://doi.org/10.1088/0004-637X/737/1/12)
- Leroy, A. K., Sandstrom, K., Rosolowsky, E., et al. 2022, arXiv e-prints, arXiv:2212.10574, <https://arxiv.org/abs/2212.10574>
- Levesque, E. M., Kewley, L. J., & Larson, K. L. 2010, *AJ*, 139, 712, doi: [10.1088/0004-6256/139/2/712](https://doi.org/10.1088/0004-6256/139/2/712)
- Long, K. S., Kuntz, K. D., Blair, W. P., et al. 2014, *ApJS*, 212, 21, doi: [10.1088/0067-0049/212/2/21](https://doi.org/10.1088/0067-0049/212/2/21)
- Lutz, D., Kunze, D., Spoon, H. W. W., & Thornley, M. D. 1998, *A&A*, 333, L75, <https://arxiv.org/abs/astro-ph/9803314>
- Lutz, D., Sturm, E., Genzel, R., et al. 2003, *A&A*, 409, 867, doi: [10.1051/0004-6361:20031165](https://doi.org/10.1051/0004-6361:20031165)
- Madau, P. 1991, *ApJL*, 376, L33, doi: [10.1086/186096](https://doi.org/10.1086/186096)
- Madden, S. C., Poglitsch, A., Geis, N., Stacey, G. J., & Townes, C. H. 1997, *ApJ*, 483, 200, doi: [10.1086/304247](https://doi.org/10.1086/304247)
- Madden, S. C., Cormier, D., Hony, S., et al. 2020, *A&A*, 643, A141, doi: [10.1051/0004-6361/202038860](https://doi.org/10.1051/0004-6361/202038860)
- Maddox, L. A., Cowan, J. J., Kilgard, R. E., et al. 2006, *AJ*, 132, 310, doi: [10.1086/505024](https://doi.org/10.1086/505024)
- Marques-Chaves, R., Schaerer, D., Alvarez-Marquez, J., et al. 2022, arXiv e-prints, arXiv:2210.02392, <https://arxiv.org/abs/2210.02392>
- Mast, D., Díaz, R. J., & Agüero, M. P. 2006, *AJ*, 131, 1394, doi: [10.1086/499941](https://doi.org/10.1086/499941)
- Meurer, G. R., Heckman, T. M., Lehnert, M. D., Leitherer, C., & Lowenthal, J. 1997, *AJ*, 114, 54, doi: [10.1086/118452](https://doi.org/10.1086/118452)
- Meurer, G. R., Heckman, T. M., Leitherer, C., et al. 1995, *AJ*, 110, 2665, doi: [10.1086/117721](https://doi.org/10.1086/117721)
- Oliva, E., Lutz, D., Drapatz, S., & Moorwood, A. F. M. 1999a, *A&A*, 341, L75, doi: [10.48550/arXiv.astro-ph/9812093](https://doi.org/10.48550/arXiv.astro-ph/9812093)
- Oliva, E., Moorwood, A. F. M., Drapatz, S., Lutz, D., & Sturm, E. 1999b, *A&A*, 343, 943, doi: [10.48550/arXiv.astro-ph/9901254](https://doi.org/10.48550/arXiv.astro-ph/9901254)
- Pavesi, R., Sharon, C. E., Riechers, D. A., et al. 2018, *ApJ*, 864, 49, doi: [10.3847/1538-4357/aacb79](https://doi.org/10.3847/1538-4357/aacb79)
- Poglitsch, A., Krabbe, A., Madden, S. C., et al. 1995, *ApJ*, 454, 293, doi: [10.1086/176482](https://doi.org/10.1086/176482)
- Rieke, G. H., Wright, G. S., Böker, T., et al. 2015, *PASP*, 127, 584, doi: [10.1086/682252](https://doi.org/10.1086/682252)
- Robertson, B. E., Ellis, R. S., Furlanetto, S. R., & Dunlop, J. S. 2015, *ApJL*, 802, L19, doi: [10.1088/2041-8205/802/2/L19](https://doi.org/10.1088/2041-8205/802/2/L19)
- Robertson, B. E., Furlanetto, S. R., Schneider, E., et al. 2013, *ApJ*, 768, 71, doi: [10.1088/0004-637X/768/1/71](https://doi.org/10.1088/0004-637X/768/1/71)
- Rodrigues, I., Dottori, H., Díaz, R. J., Agüero, M. P., & Mast, D. 2009, *AJ*, 137, 4083, doi: [10.1088/0004-6256/137/5/4083](https://doi.org/10.1088/0004-6256/137/5/4083)
- Rupke, D. 2018, *Galaxies*, 6, 138, doi: [10.3390/galaxies6040138](https://doi.org/10.3390/galaxies6040138)
- Russell, T. D., White, R. L., Long, K. S., et al. 2020, *MNRAS*, 495, 479, doi: [10.1093/mnras/staa1177](https://doi.org/10.1093/mnras/staa1177)
- Saha, A., Thim, F., Tammann, G. A., Reindl, B., & Sandage, A. 2006, *ApJS*, 165, 108, doi: [10.1086/503800](https://doi.org/10.1086/503800)
- Saintonge, A., Catinella, B., Tacconi, L. J., et al. 2017, *ApJS*, 233, 22, doi: [10.3847/1538-4365/aa97e0](https://doi.org/10.3847/1538-4365/aa97e0)
- Sakamoto, K., Matsushita, S., Peck, A. B., Wiedner, M. C., & Iono, D. 2004, *ApJL*, 616, L59, doi: [10.1086/420845](https://doi.org/10.1086/420845)
- Sandstrom, K. M., Leroy, A. K., Walter, F., et al. 2013, *ApJ*, 777, 5, doi: [10.1088/0004-637X/777/1/5](https://doi.org/10.1088/0004-637X/777/1/5)
- Sandstrom, K. M., Koch, E. W., Leroy, A. K., et al. 2022, arXiv e-prints, arXiv:2212.11177, <https://arxiv.org/abs/2212.11177>
- Savage, B. D., & Sembach, K. R. 1996, *ARA&A*, 34, 279, doi: [10.1146/annurev.astro.34.1.279](https://doi.org/10.1146/annurev.astro.34.1.279)
- Schaerer, D., Fragos, T., & Izotov, Y. I. 2019, *A&A*, 622, L10, doi: [10.1051/0004-6361/201935005](https://doi.org/10.1051/0004-6361/201935005)
- Senchyna, P., Stark, D. P., Mirocha, J., et al. 2020, *MNRAS*, 494, 941, doi: [10.1093/mnras/staa586](https://doi.org/10.1093/mnras/staa586)
- Smith, J. D. T., Draine, B. T., Dale, D. A., et al. 2007, *ApJ*, 656, 770, doi: [10.1086/510549](https://doi.org/10.1086/510549)
- Stierwalt, S., Armus, L., Charmandaris, V., et al. 2014, *ApJ*, 790, 124, doi: [10.1088/0004-637X/790/2/124](https://doi.org/10.1088/0004-637X/790/2/124)
- Sturm, E., Lutz, D., Verma, A., et al. 2002, *A&A*, 393, 821, doi: [10.1051/0004-6361:20021043](https://doi.org/10.1051/0004-6361:20021043)
- Sturm, E., Rupke, D., Contursi, A., et al. 2006, *ApJL*, 653, L13, doi: [10.1086/510381](https://doi.org/10.1086/510381)
- Tacconi, L. J., Genzel, R., & Sternberg, A. 2020, *ARA&A*, 58, 157, doi: [10.1146/annurev-astro-082812-141034](https://doi.org/10.1146/annurev-astro-082812-141034)
- Tacconi, L. J., Genzel, R., Neri, R., et al. 2010, *Nature*, 463, 781, doi: [10.1038/nature08773](https://doi.org/10.1038/nature08773)
- Thatte, N., Tecza, M., & Genzel, R. 2000, *A&A*, 364, L47, <https://arxiv.org/abs/astro-ph/0009392>
- Thilker, D. A., Lee, J. C., Deger, S., et al. 2023, arXiv e-prints, arXiv:2301.00881, <https://arxiv.org/abs/2301.00881>
- Togi, A., & Smith, J. D. T. 2016, *ApJ*, 830, 18, doi: [10.3847/0004-637X/830/1/18](https://doi.org/10.3847/0004-637X/830/1/18)
- Verma, A., Lutz, D., Sturm, E., et al. 2003, *A&A*, 403, 829, doi: [10.1051/0004-6361:20030408](https://doi.org/10.1051/0004-6361:20030408)

- Vizgan, D., Greve, T. R., Olsen, K. P., et al. 2022, *ApJ*, 929, 92, doi: [10.3847/1538-4357/ac5cba](https://doi.org/10.3847/1538-4357/ac5cba)
- Wang, Q. D., Zeng, Y., Bogdán, Á., & Ji, L. 2021, *MNRAS*, 508, 6155, doi: [10.1093/mnras/stab2997](https://doi.org/10.1093/mnras/stab2997)
- Werner, M. W., Uchida, K. I., Sellgren, K., et al. 2004, *ApJS*, 154, 309, doi: [10.1086/422413](https://doi.org/10.1086/422413)
- Williams, S. J., Bonanos, A. Z., Whitmore, B. C., Prieto, J. L., & Blair, W. P. 2015, *A&A*, 578, A100, doi: [10.1051/0004-6361/201525696](https://doi.org/10.1051/0004-6361/201525696)
- Winkler, P. F., Long, K. S., Blair, W. P., & Points, S. D. 2022, arXiv e-prints, arXiv:2212.00097. <https://arxiv.org/abs/2212.00097>
- Wofford, A., Leitherer, C., & Chandar, R. 2011, *ApJ*, 727, 100, doi: [10.1088/0004-637X/727/2/100](https://doi.org/10.1088/0004-637X/727/2/100)
- Wolfire, M. G., Hollenbach, D., & McKee, C. F. 2010, *ApJ*, 716, 1191, doi: [10.1088/0004-637X/716/2/1191](https://doi.org/10.1088/0004-637X/716/2/1191)
- Wu, R., Madden, S. C., Galliano, F., et al. 2015, *A&A*, 575, A88, doi: [10.1051/0004-6361/201423847](https://doi.org/10.1051/0004-6361/201423847)
- Yuan, Y., Krumholz, M. R., & Martin, C. L. 2022, arXiv e-prints, arXiv:2204.05006. <https://arxiv.org/abs/2204.05006>
- Zhang, D. 2018, *Galaxies*, 6, 114, doi: [10.3390/galaxies6040114](https://doi.org/10.3390/galaxies6040114)
- Zhang, Z.-Y., Romano, D., Ivison, R. J., Papadopoulos, P. P., & Matteucci, F. 2018, *Nature*, 558, 260, doi: [10.1038/s41586-018-0196-x](https://doi.org/10.1038/s41586-018-0196-x)